Influence of a density increase on the evolution of the Kelvin–Helmholtz instability and vortices

Cite as: Phys. Plasmas **17**, 072901 (2010); https://doi.org/10.1063/1.3453705
Submitted: 31 March 2010 . Accepted: 04 May 2010 . Published Online: 12 July 2010

U. V. Amerstorfer, N. V. Erkaev, U. Taubenschuss, and H. K. Biernat

Influence of a density increase on the evolution of the Kelvin–Helmholtz instability and vortices

U. V. Amerstorfer,[1] N. V. Erkaev,[2,3] U. Taubenschuss,[4] and H. K. Biernat[1,5]
[1]*Space Research Institute, Austrian Academy of Sciences, 8042 Graz, Austria*
[2]*Siberian Federal University, 660041 Krasnoyarsk, Russia*
[3]*Institute of Computational Modelling, 660036 Krasnoyarsk, Russia*
[4]*Department of Physics and Astronomy, University of Iowa, Iowa City, Iowa 52242-1479, USA*
[5]*Institute of Physics, Karl-Franzens-University Graz, 8010 Graz, Austria*

(Received 31 March 2010; accepted 4 May 2010; published online 12 July 2010)

Results of two-dimensional nonlinear numerical simulations of the magnetohydrodynamic Kelvin–Helmholtz instability are presented. A boundary layer of a certain width is assumed, which separates the plasma in the upper layer from the plasma in the lower layer. A special focus is given on the influence of a density increase toward the lower layer. The evolution of the Kelvin–Helmholtz instability can be divided into three different phases, namely, a linear growth phase at the beginning, followed by a nonlinear phase with regular structures of the vortices, and finally, a turbulent phase with nonregular structures. The spatial scales of the vortices are about five times the initial width of the boundary layer. The considered configuration is similar to the situation around unmagnetized planets, where the solar wind (upper plasma layer) streams past the ionosphere (lower plasma layer), and thus the plasma density increases toward the planet. The evolving vortices might detach around the terminator of the planet and eventually so-called plasma clouds might be formed, through which ionospheric material can be lost. For the special case of a Venus-like planet, loss rates are estimated, which are of the order of estimated loss rates from observations at Venus. © *2010 American Institute of Physics*. [doi:10.1063/1.3453705]

I. INTRODUCTION

The Kelvin–Helmholtz (KH) instability arises when layers of a stratified fluid or plasma have relative tangential velocities to each other. Such configurations occur in a variety of space plasmas, and many theoretical investigations have been performed for different regions of applications.[1–10] An extensive list of references was given, for example, by Miura.[11] One of the most prominent occurrences of the KH instability in space plasmas is at Earth's magnetopause, and hence, many of the studies focus on this topic. At unmagnetized planets, the solar wind is diverted around the ionosphere, and, as a consequence, a velocity shear is set up between the magnetosheath plasma and the ionospheric particles. This configuration should thus also be in favor of the development of the KH instability at the boundary between the two plasma layers. When approaching an unmagnetized planet, the mass density of the plasma increases due to a dense ionosphere, whereas the magnetic field decreases due to the lack of a (strong) intrinsic magnetic field of the planet. This situation differs from that at Earth or any other magnetized planet, and studies of the KH instability for such a configuration are rare.[12–17] In our solar system, we have two unmagnetized planets where it is believed that the KH instability can develop, namely, Venus and Mars. Both have been visited by a number of spacecrafts to study the plasma environment, the solar wind interaction, and involved processes.

Pioneer Venus Orbiter (PVO) observations indicate the existence of waves at the ionopause of Venus, which might hint at the development of instabilities—preferably the KH instability.[18,19] Recent analyses of Venus Express magnetometer measurements show vortices in the magnetic field, which are thought be the result of nonlinear waves at the ionopause.[20]

Recently, Gunell *et al.*[21] inferred oscillations in the electron and ion densities as well as in the ion velocity inside the induced magnetosphere of Mars from ASPERA-3 measurements. These observations were compared with one-dimensional magnetohydrodynamic (MHD) computations of the linear KH instability, and some reasonable agreements were achieved. However, the simplified one-dimensional linear model could only explain the observations partially. Consequently, further parameter studies were conducted, including also finite Larmor radius effects and variations of the parameters around the observations.[22]

From a theoretical point of view, previous studies and numerical simulations show that the KH instability might be able to develop in the vicinity of Venus[13–17] and Mars.[21,22] Some of these studies use analytical approaches, some are based on global simulations, and others focus on the linear evolution of the instability. At Venus, there are indications that the arising instability can be connected to the occurrence of plasma clouds above the ionopause,[12,14,18] which might play an important role in the erosion of the ionosphere. Brace *et al.*[18] estimated loss rates due to plasma clouds at Venus ranging from 1.4×10^{26} to 7×10^{26} ions/s. These loss rates would form a significant contribution to the loss of particles from Venus. However, in these estimations there are a number of uncertainties, as there are the sizes, shapes, velocities, and distributions of the plasma clouds as well as the composition of the plasma inside a cloud.

The KH instability might be an important process not

only for the understanding of the dynamics of the solar wind interaction with unmagnetized planets, but also for the evolution of the planetary environment, including the atmosphere and the ionosphere. The processes involved in the formation of plasma clouds and responsible for the loss of particles are not well understood at the moment.

In this paper, we study the nonlinear evolution of the KH instability, where we use plasma parameter profiles that are appropriate for unmagnetized planets. We focus our study on the application to the unmagnetized planets in our solar system because observations, which indicate the existence of waves and vortices at the boundary layer between the magnetosheath and the ionosphere, are available at these planets. Our results are also applicable to any unmagnetized planet passed by a stellar wind, where the mass density increases and the magnetic field decreases toward the planet.

The paper is organized as follows. In Sec. II we list the used MHD equations, and in Sec. III, we outline the initial configuration. The numerical method is described briefly in Sec. IV. In Sec. V we present our numerical results. We discuss the results and draw conclusions in Sec. VI.

II. MHD EQUATIONS

The conservative form of the MHD equations represents the conservation of mass, momentum, total energy, and induction of the magnetic field. This conservative system of equations can be written as

$$\frac{\partial}{\partial t}\rho + \nabla \cdot (\rho \mathbf{v}) = 0, \tag{1}$$

$$\frac{\partial}{\partial t}(\rho \mathbf{v}) + \nabla \cdot \left(\rho \mathbf{v}\mathbf{v} + \Pi \mathbf{I} - \frac{\mathbf{B}\mathbf{B}}{\mu_0}\right) = 0, \tag{2}$$

$$\frac{\partial}{\partial t}e + \nabla \cdot \left[(e + \Pi)\mathbf{v} - \frac{(\mathbf{B} \cdot \mathbf{v})\mathbf{B}}{\mu_0}\right] = 0, \tag{3}$$

$$\frac{\partial}{\partial t}\mathbf{B} + \nabla \cdot (\mathbf{v}\mathbf{B} - \mathbf{B}\mathbf{v}) = 0, \tag{4}$$

where ρ is the mass density, $\mathbf{v}$ is the plasma velocity, $\mathbf{B}$ is the magnetic field, e is the total energy density, Π is the total pressure, and μ_0 is the permeability in vacuum. The total energy density e is given by

$$e = \frac{p}{\gamma - 1} + \frac{\rho \mathbf{v}^2}{2} + \frac{\mathbf{B}^2}{2\mu_0}, \tag{5}$$

which is the sum of thermal, kinetic, and magnetic energies, with γ as the ratio of specific heats (in MHD, often an ideal gas with adiabatic change of state is assumed, thus $\gamma = 5/3$). The total pressure Π is the sum of thermal and magnetic pressures,

$$\Pi = p + \frac{\mathbf{B}^2}{2\mu_0}. \tag{6}$$

At the base of these equations lies the divergence-free condition of the magnetic field,

$$\nabla \cdot \mathbf{B} = 0. \tag{7}$$

The system of MHD equations can be rewritten in a general conservative form as

$$\frac{\partial \mathbf{U}}{\partial t} + \nabla \cdot \mathcal{F}(\mathbf{U}) = 0, \tag{8}$$

where $\mathbf{U}$ denotes the vector of conservative variables, and $\mathcal{F}(\mathbf{U})$ contains the flux vectors in all three space dimensions. In a two-dimensional (2D) Cartesian coordinate system, which we use in our study, this representation takes the form

$$\frac{\partial \mathbf{U}}{\partial t} + \frac{\partial \mathbf{F}(\mathbf{U})}{\partial x} + \frac{\partial \mathbf{G}(\mathbf{U})}{\partial y} = 0, \tag{9}$$

with the vectors

$$\mathbf{U} = \begin{pmatrix} \rho v_x \\ \rho v_y \\ \rho v_z \\ \rho \\ e \\ B_x \\ B_y \\ B_z \end{pmatrix},$$

$$\mathbf{F} = \begin{pmatrix} \rho v_x^2 + \Pi - \frac{B_x^2}{\mu_0} \\ \rho v_x v_y - \frac{B_x B_y}{\mu_0} \\ \rho v_x v_z - \frac{B_x B_z}{\mu_0} \\ \rho v_x \\ (e + \Pi) v_x - B_x (B_x v_x + B_y v_y + B_z v_z) \\ 0 \\ v_x B_y - v_y B_x \\ v_x B_z - v_z B_x \end{pmatrix}, \tag{10}$$

$$\mathbf{G} = \begin{pmatrix} \rho v_y v_x - \frac{B_y B_x}{\mu_0} \\ \rho v_y^2 + \Pi - \frac{B_y^2}{\mu_0} \\ \rho v_y v_z - \frac{B_y B_z}{\mu_0} \\ \rho v_y \\ (e + \Pi) v_y - B_y (B_x v_x + B_y v_y + B_z v_z) \\ v_y B_x - v_x B_y \\ 0 \\ v_y B_z - v_z B_y \end{pmatrix}.$$

In the numerical procedure we work with normalized quantities, such as

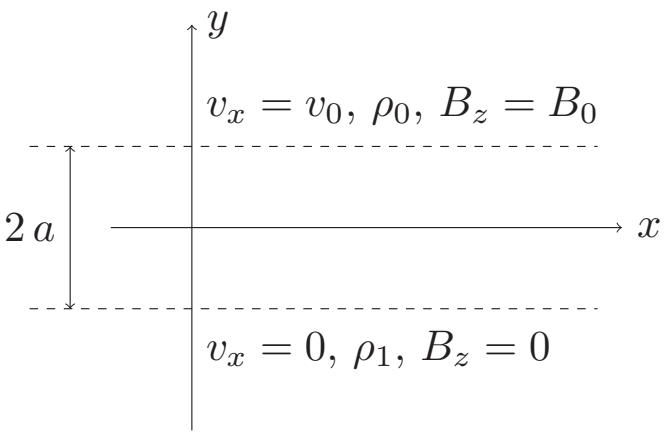

FIG. 1. Sketch of the assumed configuration. The dashed lines frame the transition layer and a denotes the half width of this layer.

$$\tilde{\rho} = \frac{\rho}{\rho_n}, \quad \tilde{\mathbf{v}} = \frac{\mathbf{v}}{v_n}, \quad \tilde{\Pi} = \frac{\Pi}{\rho_n v_n^2}, \quad \tilde{\mathbf{B}} = \frac{\mathbf{B}}{\sqrt{\mu_0 \rho_n v_n^2}}. \tag{11}$$

Subscript n denotes the dimensional quantities used for normalization. The spatial scales are normalized with a, which is the half width of the layer across which the plasma changes its properties, and the time is normalized with a/v_n. In the following, we will skip the tilde for better readability.

III. INITIAL PROFILES

We assume a boundary layer between two plasmas, across which the plasma changes its properties. When applying this situation to the solar wind interaction with unmagnetized planets, this means that the plasma changes from solar windlike to ionosphericlike across the boundary layer. Our 2D configuration is such that the x axis is along and the y axis is perpendicular to the boundary layer. Figure 1 shows a sketch of the assumed configuration. The z component of the velocity and the x and y components of the magnetic field are neglected, resulting in a configuration where the flow velocity is perpendicular to the magnetic field. Pope *et al.*[20] reported that "…the direction of the magnetic field was almost perpendicular to the plasma streamlines" in the time interval during which they observed vortices at Venus.

We assume that the plasma parameters are functions of y. Then, the initial total pressure has to satisfy the following condition to provide an initial equilibrium:

$$\frac{\partial \Pi}{\partial y} = 0. \tag{12}$$

For the calculations in this study, the following initial configuration was assumed:

$$\begin{aligned} v_x(y) &= 0.5 v_0 [1 + \tanh(y)], \\ \rho(y) &= 0.5 \rho_0 [1 + \tanh(y)] + 0.5 \rho_1 [1 - \tanh(y)], \\ B_z(y) &= 0.5 B_0 [1 + \tanh(y)], \end{aligned} \tag{13}$$

where v_0, ρ_0, and B_0 denote the (normalized) velocity, mass density, and magnetic field in the upper layer, respectively, and ρ_1 is the (normalized) mass density in the lower layer. In the lower layer, the x component of the velocity as well as the z component of the magnetic field approach zero. This represents the situation around unmagnetized planets, where the ionospheric ions can be seen to be at rest compared to the solar wind and where the planetary magnetic field can also be neglected compared to the magnetic field in the magnetosheath.

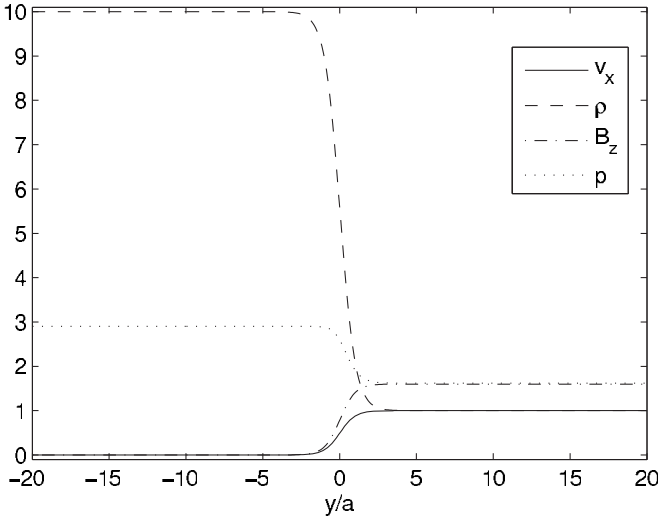

FIG. 2. Initial profiles for the $\rho_1 = 10$ case.

The initial total pressure Π is constant to fulfill Eq. (12). The initial plasma pressure is calculated from

$$p(y) = \Pi - \frac{B_z^2(y)}{2}.$$

The y component of the velocity provides the seed perturbation for the KH instability,

$$v_y(x,y) = \delta v_y \sin\left(\frac{2\pi}{L_x} x\right) e^{-y^2}, \tag{14}$$

where δv_y is the amplitude of the initial perturbation and L_x is the length of the computational box in x direction. We assume that the perturbations propagate only in x direction. Thus, we get the most unstable case, i.e., the wave number $k = k_x$ is perpendicular to the magnetic field B_z.

For this study, the following normalized values are taken as input parameters: $v_0 = 1.0$, $\rho_0 = 1.0$, $B_0 = 1.5$, $\Pi = 3.0$, and $\delta v_y = 0.01$. To investigate the influence of a dense lower plasma layer on the evolution and vortex formation of the KH instability, the mass density of the lower region is varied. We present results for different values of $\rho_1 = 10/50/100$, meaning that the densities in the lower plasma layer are 10, 50, and 100 times larger than the density in the upper layer, respectively. Such large density variations occur around unmagnetized planets when the planetary ionosphere is approached. The initial profiles for the case with $\rho_1 = 10$ are shown in Fig. 2 as an example of the profiles.

IV. NUMERICAL METHOD

In many situations, the MHD system can become very complex: On the one hand, there can be steep gradients, shock waves, or other discontinuities, and on the other hand, there can simultaneously be smooth flows away from discontinuities. So, it would be desirable to have numerical schemes of high order for the smooth flows, while at the same time it would be desirable to have numerical schemes that are capable of resolving discontinuities without spurious oscillations. These properties are combined in the so-called total variation diminishing (TVD) schemes introduced by Harten.[23] Resolving discontinuities means solving a Riemann problem and many TVD schemes use exact or approximate Riemann solvers. For the use of Riemann solvers, the local characteristic waves are needed. This makes the implementation rather complex and the application is restricted to one specific set of equations with specific eigenvectors and eigenvalues. However, Yee[24] showed that there is the possibility to have a second-order TVD scheme without the need to use a Riemann solver—the so-called TVD Lax–Friedrichs (TVDLF) scheme. This scheme is described and tested by Tóth and Odstrčil,[25] and we give only a brief overview of the most important points.

In the following, U denotes the vector of conserved variables and F the flux vector. The cells of the mesh are centered at positions x_i, where cell interfaces are denoted by $x_{i-1/2}$ and $x_{i+1/2}$, with $x_{i+1/2}=0.5(x_i+x_{i+1})$. U_i^n represent the volume-averaged discretized conserved variables at time level t^n within the ith cell. The time marching scheme of the TVDLF algorithm in one dimension is given by

$$U_i^{n+1} = U_i^n - \frac{\Delta t}{\Delta x}(F_{i+1/2}^{\mathrm{TVDLF}} - F_{i-1/2}^{\mathrm{TVDLF}}), \tag{15}$$

with $\Delta t=t^{n+1}-t^n$ as the time step and $\Delta x=x_{i+1}-x_i$ as the space step. The task lies in finding the appropriate fluxes at the cell interfaces, i.e., $F_{i+1/2}^{\mathrm{TVDLF}}$ and $F_{i-1/2}^{\mathrm{TVDLF}}$. These intercell fluxes are defined as

$$F_{i+1/2}^{\mathrm{TVDLF}} = F_{i+1/2}^{LR} - \tfrac{1}{2}c_{i+1/2}^{\max}\Delta U_{i+1/2}^{LR}, \tag{16}$$

where

$$\begin{aligned} F_{i+1/2}^{LR} &= 0.5[F(U_{i+1/2}^L) + F(U_{i+1/2}^R)], \\ \Delta U_{i+1/2}^{LR} &= U_{i+1/2}^R - U_{i+1/2}^L, \end{aligned} \tag{17}$$

and superscripts L and R denote the left and right states of the local Riemann problem, respectively. Quantity $c_{i+1/2}^{\max}$ is the maximum propagation speed of information on the mesh, which is the sum of the macroscopic flow velocity and the fast magnetoacoustic wave,

$$c_d^{\max} = |v_d| + \frac{1}{\sqrt{2}}\sqrt{\frac{\gamma p + \mathbf{B}^2}{\rho} + \sqrt{\left(\frac{\gamma p + \mathbf{B}^2}{\rho}\right)^2 - 4\frac{\gamma p}{\rho}\frac{B_d^2}{\rho}}}, \tag{18}$$

where $d=x,y$ denotes the spatial dimension. Following the suggestion of Tóth and Odstrčil,[25] we take $c_{i+1/2}^{\max}=c_x^{\max}(U^{LR})$. The left and right states are given by

$$\begin{aligned} U_{i+1/2}^L &= U_i^{n+1/2} + \tfrac{1}{2}\overline{\Delta U}_i^n, \\ U_{i+1/2}^R &= U_{i+1}^{n+1/2} - \tfrac{1}{2}\overline{\Delta U}_{i+1}^n, \end{aligned} \tag{19}$$

where $U_i^{n+1/2}$ are the variables at intermediate time levels $t^{n+1/2}$ and $\overline{\Delta U}_i^n$ are the limited differences of the conserved variables. Different limiters exist with different properties, e.g., the minmod limiter, which is very diffusive, or the superbee limiter, which is rather sharp. A limiter in between these two is the woodward limiter, which is defined as[25]

$$\begin{aligned} \overline{\Delta U}_i = \mathrm{sgn}(2\Delta U_{i-1/2})\max\{0, \min[&|2\Delta U_{i-1/2}|, \\ &\mathrm{sgn}(2\Delta U_{i-1/2})2\Delta U_{i+1/2}, \\ &\mathrm{sgn}(2\Delta U_{i-1/2})0.5(\Delta U_{i-1/2} + \Delta U_{i+1/2})]\}, \end{aligned} \tag{20}$$

where $\Delta U_{i-1/2}=U_i-U_{i-1}$. To get the variables at intermediate time levels, a so-called Hancock predictor is used,

$$U_i^{n+1/2} = U_i^n - \frac{1}{2}\frac{\Delta t}{\Delta x}\left[F\left(U_i^n + \frac{1}{2}\overline{\Delta U}_i^n\right) - F\left(U_i^n - \frac{1}{2}\overline{\Delta U}_i^n\right)\right]. \tag{21}$$

To extend the numerical scheme to two dimensions, a Strang-type operator splitting in the following form is implemented:

$$U^{n+2} = D_x D_y D_y D_x U^n, \tag{22}$$

where D_x and D_y denote the appropriate operations in one dimension for a given time step. Very good results are achieved by alternating the order of the operators.[25] The time step Δt is updated after each dimension sweep and is restricted by the Courant–Friedrichs–Levy condition, i.e.,

$$\Delta t = C\ \min\left(\frac{\Delta d}{c_d^{\max}}\right), \tag{23}$$

where we set $C=0.8$. We use periodic boundary conditions in the x direction and fixed boundary conditions in the y direction. The computational box is taken to be $(0,L_x)\times(-20,+20)$.

V. RESULTS

A. Linear growth rates

It is well known that at the beginning of the KH instability, the perturbation grows exponentially and a linear growth rate can be determined.[6] Taking the logarithm of the peak vertical kinetic energy $E_y=0.5\rho v_y^2$ of each time step, this exponential growth manifests itself as a linear slope (see Fig. 3). The linear growth rate is obtained from the slope of a linear function fitted to the initial growth phase.

To find the wave number for the maximum growth of the instability, we varied the wave number of the seed perturbation, $k_x=2\pi/L_x$, and then calculated the linear growth rate for each k_x. The result is shown in Fig. 4. The wave number k_m, at which the maximum growth rate γ_m occurs, decreases with an increasing density jump—from $k_m a\approx 0.52$ for $\rho_1=10$ to $k_m a\approx 0.35$ for $\rho_1=100$. Also, γ_m decreases with an increasing ρ_1, which was already seen in previous studies.[16,17] Setting it into concrete values, increasing the

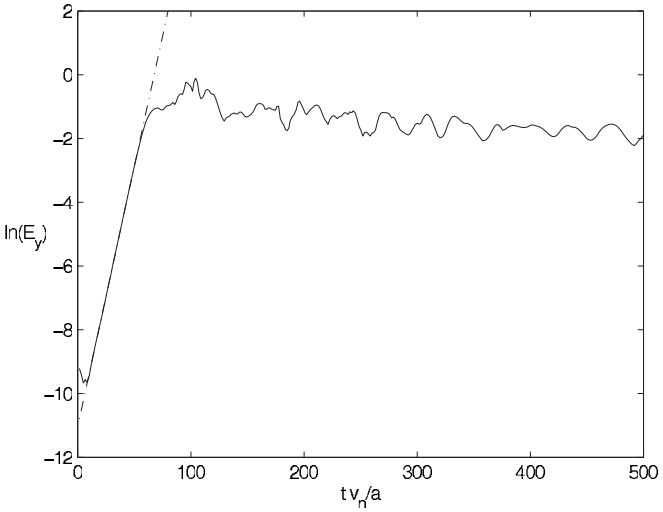

FIG. 3. Time evolution of the logarithm of the peak vertical kinetic energy E_y for the case $\rho_1=10$ and $k_x a=0.52$. The dashed-dotted line represents a linear fit.

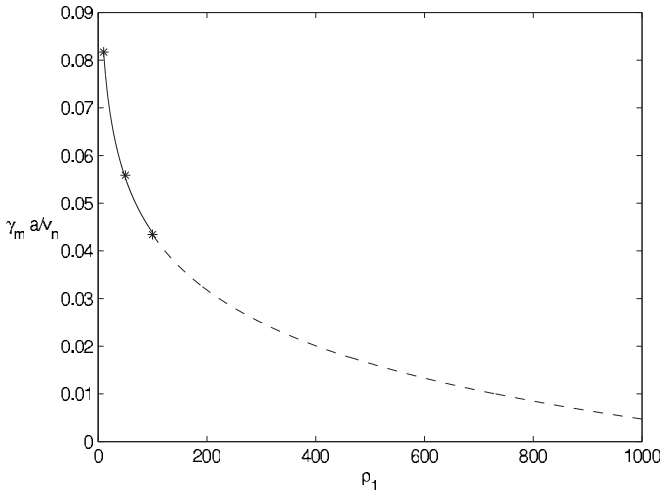

FIG. 5. Maximum growth rate as a function of the density jump ρ_1. The asterisks mark the maximum growth rates obtained numerically, whereas the solid and dashed lines represent the logarithmic fit.

density of the lower plasma layer ten times halves the maximum growth rate. We found that the dependence of γ_m on ρ_1 can be fitted by a logarithmic function of the form $\gamma_m=c+b\ln(\rho_1)$ with $c=0.1208$ and $b=-0.0168$, as displayed in Fig. 5. The dashed line in this figure represents the possible continuation of the curve for larger ρ_1.

B. Saturation and nonlinear evolution

Having determined k_m, we know at which wave number, respectively, wavelength, the KH instability has its fastest growth, and we can examine the different phases of the evolution. As already pointed out previously, the initial phase is characterized by an exponential growth of the perturbations, which we call linear growth phase since we can determine a linear growth rate for this phase. Clearly visible in Fig. 3 is a saturation after the linear growth phase. In line with the work by Keppens *et al.*,[6] we take the first maximum of the evolution of $\ln(E_y)$ as a measure of the saturation level and the corresponding linear growth time t_{lin}, which we define as the time needed for the linear growth. Figure 6 displays the evolution of $\ln(E_y)$, the saturation levels, and the linear growth times for three different cases. An increase of the density jump increases t_{lin}, which means that a vortex needs more time to evolve if the lower plasma layer has a larger density. Quantitatively, we have $t_{\mathrm{lin}}=71.1a/v_n$ for $\rho_1=10$, $t_{\mathrm{lin}}=97.6a/v_n$ for $\rho_1=50$, and $t_{\mathrm{lin}}=119.4a/v_n$ for $\rho_1=100$.

During the linear growth phase, the perturbations grow, and eventually rolled-up vortices are formed at the saturation level. Figures 7–9 show the time series of the mass density for the cases $\rho_1=10$ and $k_m a=0.52$, $\rho_1=50$ and $k_m a=0.42$, and $\rho_1=100$ and $k_m a=0.35$, respectively. The vortices become more inhomogeneous and less structured for the high density cases.

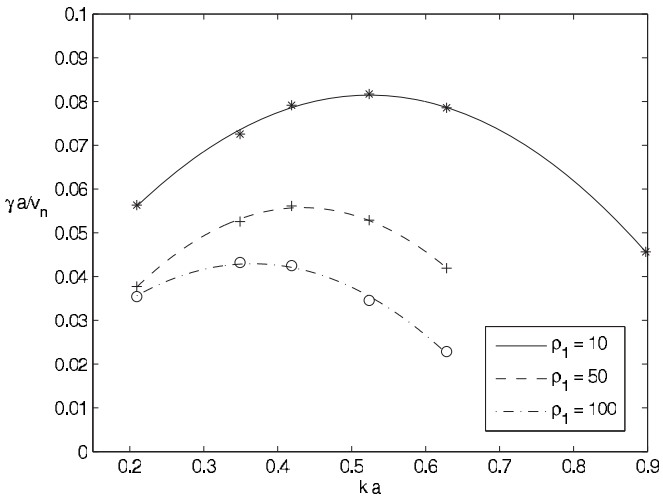

FIG. 4. Normalized linear growth rate as a function of the normalized wave number. The symbols mark the growth rates obtained numerically, whereas the solid, dashed, and dashed-dotted lines represent parabolic fits.

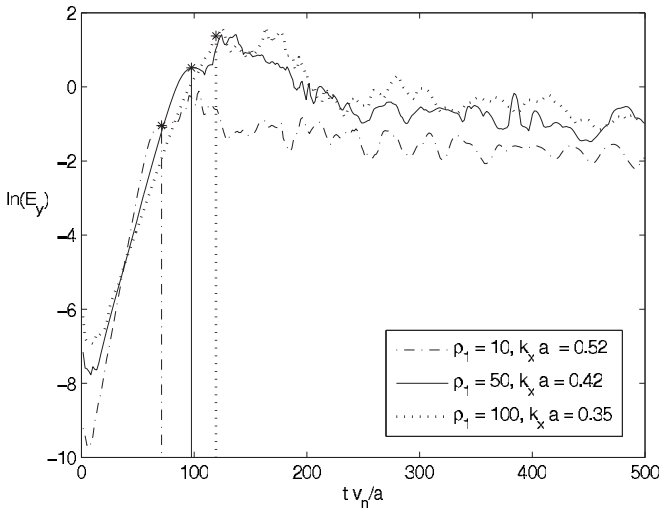

FIG. 6. Time evolution of the logarithm of the peak vertical kinetic energy E_y for three different cases. The asterisks and the vertical lines highlight the first maximum of $\ln(E_y)$ and the corresponding linear growth time, respectively.

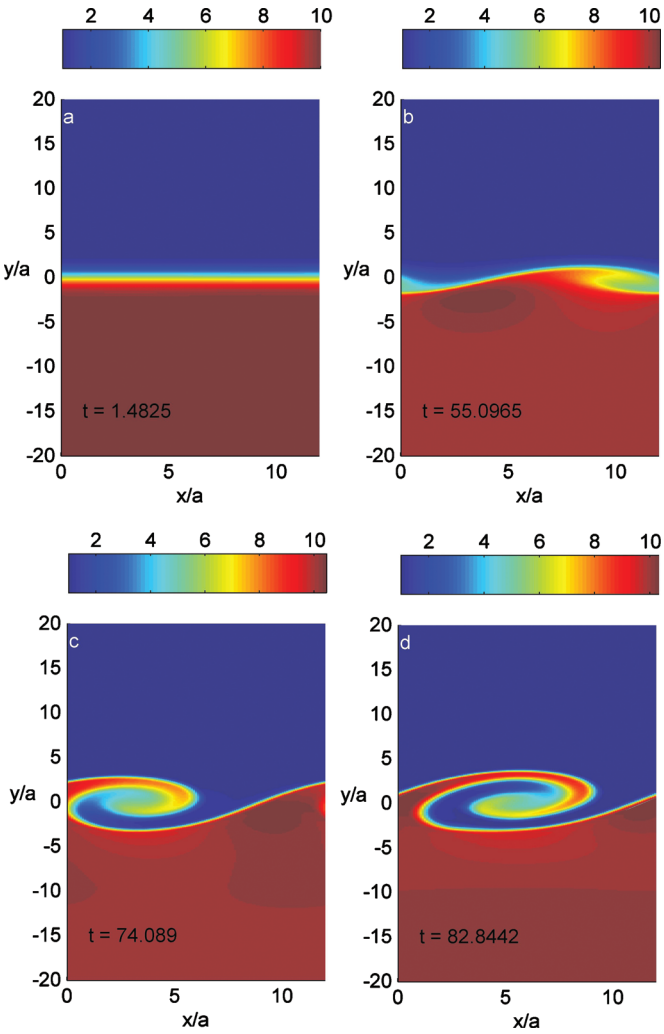

FIG. 7. (Color) Evolution of the density for $\rho_1=10$ and $k_m a=0.52$ (enhanced online). [URL: http://dx.doi.org/10.1063/1.3453705.1]

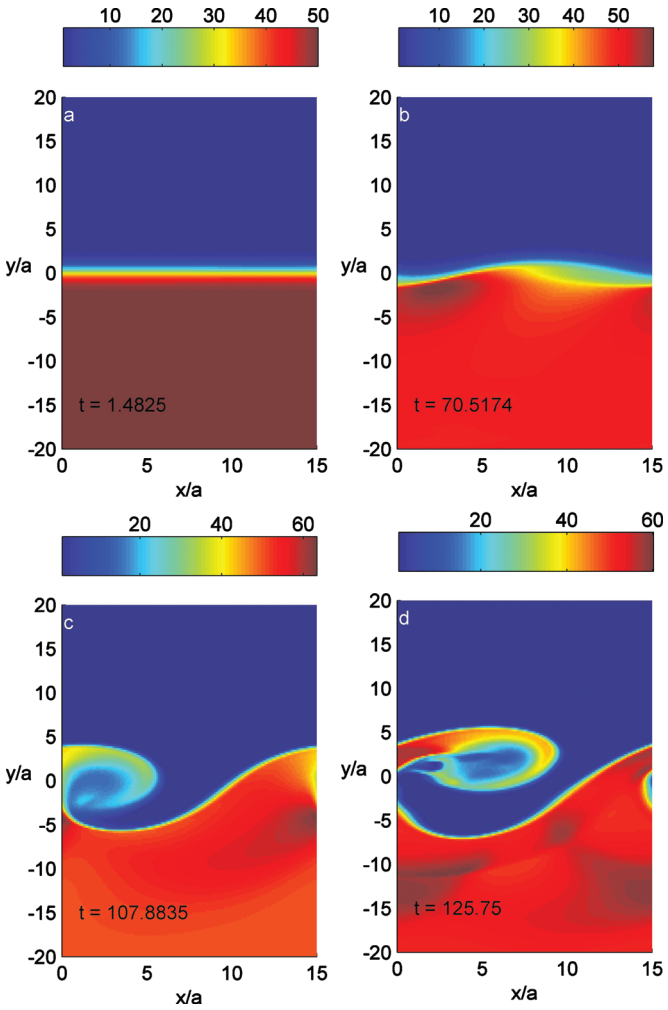

FIG. 8. (Color) Evolution of the density for $\rho_1=50$ and $k_m a=0.42$.

After saturation is reached and the vortices are developed, the boundary layer becomes more and more turbulent, and no regular structures can be observed anymore (see Fig. 10). At this stage of the nonlinear evolution of the KH instability, the boundary layer is broken up and has a width of approximately $10a$.

VI. DISCUSSION AND CONCLUSIONS

There are some important features to emphasize. We can distinguish three phases in the evolution of the KH instability:

(1) linear growth phase,
(2) nonlinear phase with a regular structure of the vortices, and
(3) turbulent phase with nonregular structures.

The average velocity of the perturbations along the x axis is about $0.5v_n$. From this, we can estimate the travel distance D of the perturbation along the boundary layer during the linear growth time t_{lin},

$$D = \frac{v_n}{2} t_{\text{lin}}. \tag{24}$$

In other words, the perturbations need the distance D to grow to vortices. Inserting the appropriate values for t_{lin}, we get

$$D_{10} \approx 36a,$$

$$D_{50} \approx 49a, \tag{25}$$

$$D_{100} \approx 60a,$$

where D_{10}, D_{50}, and D_{100} are the travel distances for the different ρ_1 cases. The travel distance does not depend on v_n because the velocity cancels out due to the normalization of time.

An interesting point is that the maximum growth rate γ_m multiplied by the corresponding linear growth time t_{lin} gives approximately 5.5 for each of the three cases. So, having either the growth rate or the growth time, one can estimate the other from this relation.

As can be seen from Figs. 7–9, the spatial scale of the vortices, L_V, in x as well as in y direction is approximately $10a$. Taking the half width of the boundary layer as $a=50$ km, which, for example, is a value found at Venus,[26] we

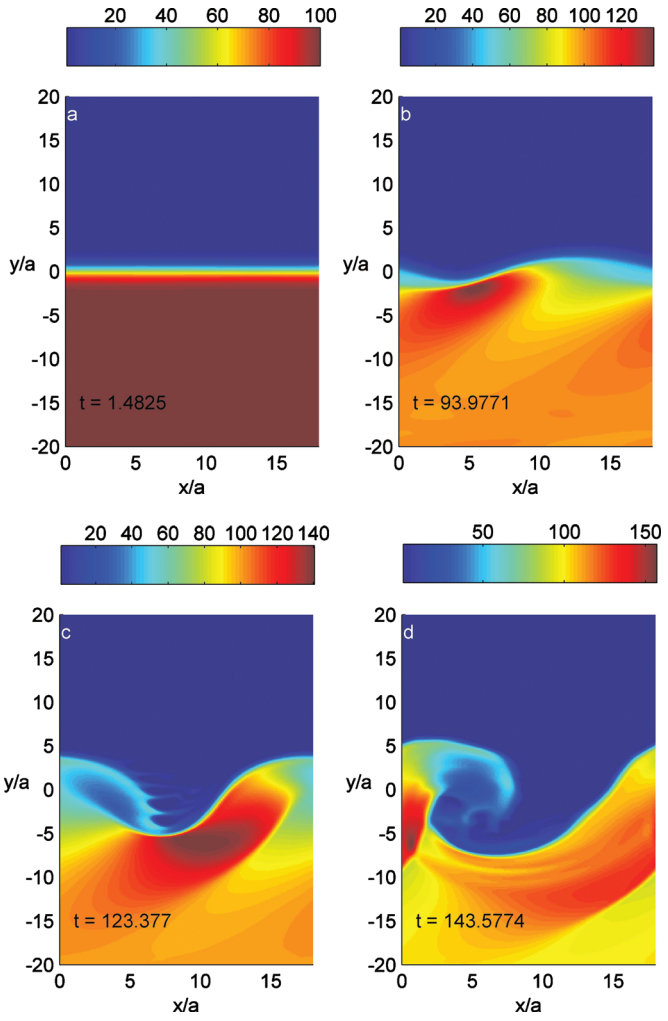

FIG. 9. (Color) Evolution of the density for $\rho_1=100$ and $k_m a=0.35$.

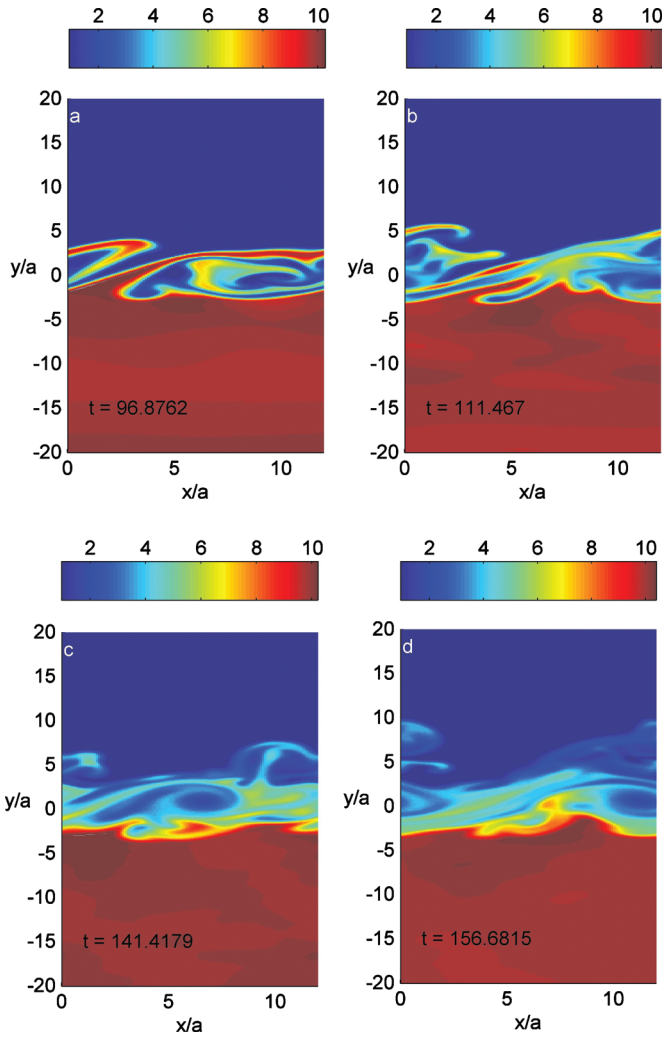

FIG. 10. (Color) Evolution of the density for $\rho_1=10$ and $k_m a=0.52$ into turbulent phase.

have $D_{10}=1800$ km, $D_{50}=2450$ km, $D_{100}=3000$ km, and $L_V=500$ km. The distance from a planet's subsolar point to the terminator is about $L_0=(\pi/2)R_{\rm pl}$, where $R_{\rm pl}$ is the radius of the planet. For Venus and Mars, for example, we have $L_0\approx 9500$ km and $L_0\approx 5300$ km, respectively, both of which are larger than the travel distances D_{10}, D_{50}, and D_{100} of the perturbations on their way along the boundary layer. Thus, the perturbations can reach the nonlinear phase during their propagation from the subsolar point to the terminator.

At Venus, detached plasma structures, termed plasma clouds, were observed above the ionopause by PVO.[18] It is thought that they are the final stage of the KH instability and that they contain ionospheric particles which are lost to the solar wind. Estimations of loss rates due to this process were given by Brace *et al.*[18] and range from 1.4×10^{26} to 7×10^{26} ions/s.

From our simulation results, we can obtain a theoretical estimation of the loss rate. We consider the case of density $\rho_1=100$. In this case, the initially small perturbations reach the nonlinear stage during time $t_{\rm lin}\approx 120a/v_n$. The spatial scale of the vortex is $L_V\approx 10a$ in both x and y directions. The shape of the perturbation can be roughly approximated by

$$y(x)=L_V\sin^2\left(\pi\frac{x}{L_V}\right), \tag{26}$$

where $0<x<L_V$. The amount of ionospheric particles involved in one cloud, $N_{\rm cloud}$, can then be estimated as

$$N_{\rm cloud}\sim n_1 l_z\int_0^{L_V} y(x)dx\sim 0.5 n_1 L_V^2 l_z, \tag{27}$$

where n_1 is the number density in the ionosphere and l_z represents the scale of the cloud along the terminator, which is also along the magnetic field (which is perpendicular to the plasma flow). Each zone produces a cloud within time $t_{\rm lin}$, thus the loss rate due to one cloud, $\Gamma_{\rm cloud}$, is obtained by

$$\Gamma_{\rm cloud}=\frac{N_{\rm cloud}}{t_{\rm lin}}. \tag{28}$$

To get the total number of clouds, we split the area along the terminator in different zones, each of which corresponds to

one cloud and has the size l_z. The number of zones/clouds in one hemisphere is then given by

$$K = \frac{\pi R_{\mathrm{pl}}}{l_z}. \tag{29}$$

If we exclude the zones where the magnetic field is not perpendicular to the plasma flow, the actual number of clouds is smaller, and we roughly assume

$$K^* = \frac{2R_{\mathrm{pl}}}{l_z} < K. \tag{30}$$

For the total loss rate Γ, we multiply Γ_{cloud} by K^* and by 2 (for the two hemispheres), and thus, we get

$$\Gamma = 2K^*\Gamma_{\mathrm{cloud}} = \frac{4R_{pl}N_{\mathrm{cloud}}}{l_z t_{\mathrm{lin}}} = \frac{5}{3} n_1 R_{\mathrm{pl}} v_n a. \tag{31}$$

Assuming parameters for a Venus-like planet, such as $R_{\mathrm{pl}}=6\times10^3$ km, $v_n=400$ km/s, $a=50$ km, and $n_1=1000$ cm^{-3}, we find the loss rate $\Gamma=2\times10^{26}$ ions/s. This theoretical loss rate is of the same order as that estimated from observations.[18]

There are two main factors which have a substantial influence on the loss rate: the solar wind velocity and the plasma density. An enhancement of the velocity directly leads to an increase of the particle loss rate because of proportionality. The influence of the plasma density acts indirectly through the linear growth time. For a fixed ionospheric density n_1, an increase of the solar wind density n_0 leads to a decrease of the density ratio n_1/n_0, and thus, to a decrease of the growth time t_{lin}. A decrease of the density ratio of ten times approximately halves the growth time. The most crucial effect on the loss rate might be due to a simultaneous increase of the solar wind density and velocity.

ACKNOWLEDGMENTS

This work was supported by the FWF under Project No. P21051-N16 and also by the RFBR under Grant No. 09-05-91000-ANF_a.

[1] A. I. Ershkovich, Space Sci. Rev. **25**, 3 (1980).
[2] T. P. Downes and T. P. Ray, Astron. Astrophys. **331**, 1130 (1998).
[3] M. Fujimoto and T. Terasawa, J. Geophys. Res. **96**, 15725, doi:10.1029/91JA01312 (1991).
[4] A. G. González and J. Gratton, J. Plasma Phys. **52**, 223 (1994).
[5] K. A. Keller and R. L. Lysak, J. Geophys. Res. **104**, 25097, doi:10.1029/1999JA900368 (1999).
[6] R. Keppens, G. Tóth, R. H. J. Westermann, and J. P. Goedbloed, J. Plasma Phys. **61**, 1 (1999).
[7] Y. Kobayashi, M. Kato, K. T. A. Nakamura, T. K. M. Nakamura, and M. Fujimoto, Adv. Space Res. **41**, 1325 (2008).
[8] A. Miura, Phys. Rev. Lett. **49**, 779 (1982).
[9] Z. Pu and M. G. Kivelson, J. Geophys. Res. **88**, 841, doi:10.1029/JA088iA02p00841 (1983).
[10] K. Takagi, C. Hashimoto, H. Hasegawa, M. Fujimoto, and R. TanDokoro, J. Geophys. Res. **111**, A08202, doi:10.1029/2006JA011631 (2006).
[11] A. Miura, Phys. Plasmas **4**, 2871 (1997).
[12] R. S. Wolff, B. E. Goldstein, and C. M. Yeates, J. Geophys. Res. **85**, 7697, doi:10.1029/JA085iA13p07697 (1980).
[13] R. C. Elphic and A. I. Ershkovich, J. Geophys. Res. **89**, 997, doi:10.1029/JA089iA02p00997 (1984).
[14] V. A. Thomas and D. Winske, Geophys. Res. Lett. **18**, 1943, doi:10.1029/91GL02552 (1991).
[15] N. Terada, S. Machida, and H. Shinagawa, J. Geophys. Res. **107**, 1471, doi:10.1029/2001JA009224 (2002).
[16] U. V. Amerstorfer, N. V. Erkaev, D. Langmayr, and H. K. Biernat, Planet. Space Sci. **55**, 1811 (2007).
[17] H. K. Biernat, N. V. Erkaev, U. V. Amerstorfer, T. Penz, and H. I. M. Lichtenegger, Planet. Space Sci. **55**, 1793 (2007).
[18] L. H. Brace, R. F. Theis, and W. R. Hoegy, Planet. Space Sci. **30**, 29 (1982).
[19] C. T. Russell and O. Vaisberg, in *Venus*, edited by D. M. Hunten, L. Colin, T. M. Donahue, and V. I. Moroz (University of Arizona Press, Tucson, 1983), pp. 873–940.
[20] S. A. Pope, M. A. Balikhin, T. L. Zhang, A. O. Fedorov, M. Gedalin, and S. Barabash, Geophys. Res. Lett. **36**, L07202, doi:10.1029/2008GL036977 (2009).
[21] H. Gunell, U. V. Amerstorfer, H. Nilsson, C. Grima, M. Koepke, M. Fraenz, J. D. Winningham, R. A. Frahm, J.-A. Sauvaud, A. Fedorov, N. V. Erkaev, H. K. Biernat, M. Holmstroem, R. Lundin, and S. Barabash, Plasma Phys. Controlled Fusion **50**, 074018 (2008).
[22] U. V. Amerstorfer, H. Gunell, N. V. Erkaev, and H. K. Biernat, Astrophys. Space Sci. Trans. **5**, 39 (2009).
[23] A. Harten, J. Comput. Phys. **49**, 357 (1983).
[24] H. C. Yee, "A class of high–resolution explicit and implicit shock–capturing methods," NASA Report No. TM-101088, 1989.
[25] G. Tóth and D. Odstrčil, J. Comput. Phys. **128**, 82 (1996).
[26] R. C. Elphic, C. T. Russell, J. G. Luhmann, F. L. Scarf, and L. H. Brace, J. Geophys. Res. **86**, 11430, doi:10.1029/JA086iA13p11430 (1981).